Extreme Mechanics Letters 40 (2020) 100940

Contents lists available at ScienceDirect

Extreme Mechanics Letters

journal homepage: www.elsevier.com/locate/eml

A dynamic analysis of the Rayleigh–Taylor instability in soft solids

Saiful Islam Tamim, Joshua B. Bostwick *

Department of Mechanical Engineering, Clemson University, Clemson SC 29634, United States of America

ARTICLE INFO

Article history:
Received 1 June 2020
Received in revised form 20 July 2020
Accepted 12 August 2020
Available online 19 August 2020

Keywords:
Elastocapillarity
Soft matter
Viscoelastic material
Stability and bifurcation

ABSTRACT

A soft viscoelastic layer is susceptible to interfacial instability due to self-weight when oriented in a heavy over light configuration. This is the solid Rayleigh–Taylor instability. We perform an elastodynamic stability analysis for the viscoelastic layer in a cylindrical container and compute the dispersion relationship, as it depends upon the dimensionless elastogravity number, elastocapillary number, solid Deborah number, compressibility number, and the aspect ratio. The stability diagram is mapped in the parameter space and we compute the wavenumber and associated growth rate for the dominant mode. The presence of the cylindrical boundary restricts the allowable modes and we show how this affects mode number selection. Our predictions compare favorably to previously reported experimental work in the literature.

1. Introduction

Soft materials, such as polymer-based gels and biological tissues, are susceptible to large deformations due to external loading or self-weight and this gives rise to many interesting phenomena including soft fracture [1,2], soft wetting [3–5], and surface morphological instabilities [6,7]. These materials are typically characterized by small elasticity E, such that surface tension σ becomes important in systems with length scales L larger than the elastocapillary length $\ell_e \equiv \sigma/E$, $L > \ell_e$. The study of systems for which $L \sim \ell_e$ belongs to the field of elastocapillarity [8–10]. This unique behavior of soft solids suggest they are subject to many of the classical instabilities of hydrodynamics and many of these have been recently observed in soft solids; Plateau–Rayleigh breakup of a cylinder [11,12], fingering instabilities [13], and drop oscillations [14,15]. Our focus is on the gravity-driven instability of an elastic material oriented in an adverse density gradient, the elastic analogue of the Rayleigh–Taylor instability [16,17].

Rayleigh–Taylor instability in solids is relevant to a number of diverse fields, such as geology and the density-stratified layers of the continental lithosphere [18,19], astrophysics and the explosion of supernova [20], as well as high-energy physics [21]. For this reason, much attention has been paid to this problem over the years [22–27]. Recently, Mora et al. [28] observed gravity-driven instabilities on the free surface of a soft elastic layer in a cylindrical container. Here, the competition between gravity and elasticity gave rise to undulating surface patterns beyond a threshold value for the non-dimensional elastogravity number that agreed with a theoretical prediction due to an energy analysis. Beyond threshold, finite-size deformations lead to a steady shape that has been described through nonlinear bifurcation analysis in a later work [29]. These theories assumed an incompressible solid layer of infinite horizontal extent. The effect of geometric confinement on the Rayleigh–Taylor instability in fluids is well-known [30,31] and Zheng et al. [32] have recently shown finite-size effects in soft solids. In this paper we will develop a model of Rayleigh–Taylor instability in soft solids that incorporates geometric effects, in addition to gravity, surface tension, elasticity, compressibility, and viscoelasticity.

Static stability analysis is useful in determining the overall stability of a system and the range of unstable wavenumbers when the system is unstable. However, only a dynamic stability analysis can determine the dominant mode in the system that ultimately leads to pattern formation. Boundary effects also play a large role in wavenumber selection by restricting the allowable modes. We perform a dynamic stability analysis of a linear viscoelastic layer confined laterally by a cylindrical container and compute the dispersion relationship, as it depends upon the dimensionless parameters: elastogravity number α, elastocapillary number Σ, solid Deborah number τ, compressibility number $\tilde{\nu}$, and aspect ratio $\tilde{R}$. Gravity destabilizes the interface above a threshold value of α when oriented in the classic Rayleigh–Taylor configuration of heavy over light, while surface tension stabilizes the range of unstable wavenumbers, and we compute the stability diagram in the parameter space. Each dispersion curve exhibits a single maximum and we compute the critical wavenumber and associated growth rate for this dominant mode. For a finite-sized container, we identify the range of parameters for which a given mode is the dominant mode and show there are regions

* Corresponding author.
E-mail address: jbostwi@clemson.edu (J.B. Bostwick).

https://doi.org/10.1016/j.eml.2020.100940
2352-4316/

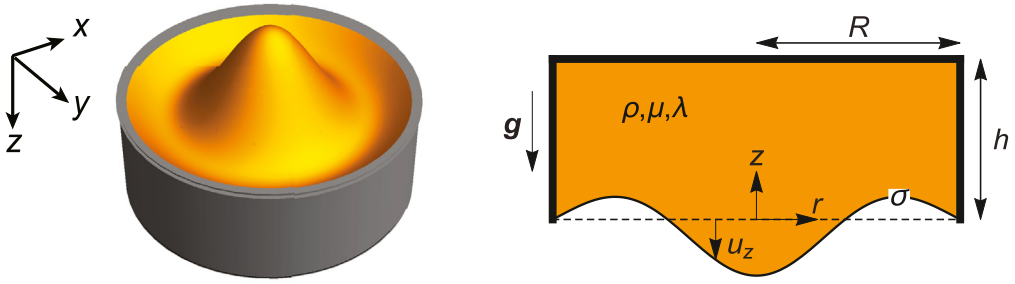

Fig. 1. Definition sketch in 3D perspective (left) and 2D projection (right) views.

which exhibit multiple dominant modes with the same growth rate. Our predictions compare favorably to previously reported experiments. Lastly, we end with some concluding remarks.

2. Mathematical formulation

Consider a soft viscoelastic layer of thickness h in cylindrical coordinates (r, θ, z), as shown in Fig. 1. The layer is rigidly bound to a container of radius R at $z = h$, has a free surface at $z = 0$ that is endowed with a surface tension σ, and is oriented such that gravity g acts from the solid through the free surface. This is sometimes referred to as negative loading, i.e. the heavy over light configuration that is required for the Rayleigh–Taylor instability. The layer has the following material properties: density ρ, Lamé parameters λ and μ, and Poisson ratio ν.

2.1. Field equations

The solid is considered to be a linearly viscoelastic material with the stress field τ_{ij} related to the strain field ε_{ij} by [33],

$$\tau_{ij}(t) = 2\int_{-\infty}^{t} \mu(t-t')\frac{\partial \varepsilon_{ij}(t')}{\partial t'}dt' + \delta_{ij}\int_{-\infty}^{t} \lambda(t-t')\frac{\partial \varepsilon_{kk}(t')}{\partial t'}dt', \quad (1)$$

where $\mu(t)$ and $\lambda(t)$ are relaxation moduli, which are related to each other through the Poisson ratio ν as, $\lambda = 2\nu/(1-2\nu)\mu$. The strain ε_{ij} is related to the three-dimensional displacement field $\mathbf{U}(r, \theta, z)$, as, $\varepsilon_{ij} = \frac{1}{2}\left(\frac{\partial U_i}{\partial x_j} + \frac{\partial U_j}{\partial x_i}\right)$. The stress tensor satisfies the equilibrium equation,

$$\frac{\partial \tau_{ij}}{\partial x_j} = \rho\frac{\partial^2 U_i}{\partial t^2}. \quad (2)$$

2.2. Normal modes and the reduced equations

Normal modes e^{st} are assumed with s is the growth rate, e.g. the displacement field is defined as $\mathbf{U} = \mathbf{u}(r, \theta, z)e^{st}$, with $\mathbf{u}(r, \theta, z) = u_r(r, \theta, z)\hat{e}_r + u_\theta(r, \theta, z)\hat{e}_\theta + u_z(r, \theta, z)\hat{e}_z$ the time-independent field. We use a two-sided Laplace transform $\tilde{f}(s) = \frac{1}{\sqrt{2\pi}}\int_{-\infty}^{\infty} f(t)e^{st}dt$ to convert from the time domain to the growth rate domain.

Applying the two-side Laplace transform to (1) yields

$$\tilde{\tau}_{ij}(s) = 2\tilde{\mu}(s)\tilde{\varepsilon}_{ij}(s) + \delta_{ij}\tilde{\lambda}(s)\tilde{\varepsilon}_{kk}(s), \quad (3)$$

where the complex shear modulus $\tilde{\mu}(s)$ is defined as

$$\tilde{\mu}(s) = \tilde{\mu}'(s) + i\tilde{\mu}''(s) = s\int_0^{\infty} \Psi(t)e^{-st}dt, \quad (4)$$

with $\tilde{\mu}'(s)$ and $\tilde{\mu}''(s)$ the storage and loss modulus, respectively. The relaxation function Ψ is determined by the rheology of the material and will be discussed shortly. For a complex solid, they are both function of the frequency or in our particular case, the unstable growth rate. In most cases, the Poisson ratio ν is considered to be constant and independent of the dynamics. Using (3) and the normal mode solution, we can write the governing equation (2) as

$$(\tilde{\lambda}(s) + \tilde{\mu}(s))\nabla(\nabla \cdot \mathbf{u}) + \tilde{\mu}(s)\nabla^2\mathbf{u} = \rho s^2\mathbf{u}. \quad (5)$$

2.3. Rheology

We assume our soft solid behaves as a power law gel where $\mu'(s)$ and $\mu''(s)$ both scale with time as t^{-n} [34,35]. Here, n is the power law exponent and its value typically range from $0.5 \sim 1$. The complex modulus for these materials can be approximated as [36],

$$\tilde{\mu}(s) = \mu\left(1 + (st_v)^n\right), \quad (6)$$

where μ is the static or reference shear modulus and t_v is the relaxation timescale. Note that $t_v = 0$ corresponds to the purely elastic limit. This is sometimes referred to as the fractional Kelvin–Voigt model, as the special case of $n = 1$ gives the classical Kelvin–Voigt model.

2.4. Boundary conditions

The boundary between the elastic layer and container $z = h$ is assumed to be rigidly bonded and no displacement conditions are enforced there,

$$u_r = u_\theta = u_z = 0. \quad (7)$$

Continuity of stress is enforced at the free surface $z = 0$,

$$\tau_{rz} = \tau_{\theta z} = 0, \quad (8a)$$

$$\tau_{zz} = -\rho g u_z + \sigma\nabla \cdot \mathbf{n}, \quad (8b)$$

where the former are the shear-free conditions and the latter is the linearized Young–Laplace equation governing the jump in normal stress across an interface with surface tension. Here $\mathbf{n}$ is the outward unit normal to the free surface and $\nabla \cdot \mathbf{n} = -(\frac{\partial^2}{\partial r^2} + \frac{1}{r}\frac{\partial}{\partial r} + \frac{1}{r^2}\frac{\partial^2}{\partial \theta^2})u_z$ is the linearized curvature there. The gravitational term accounts for the excess weight due to the free surface disturbance.

For now, we assume the layer is semi-infinite or extends to infinity in the xy plane. This simplification allows us to introduce a continuous wavenumber, which allows us to explicitly recover prior results for some limiting cases. In a later section, we introduce a lateral boundary at $r = R$, which 'quantizes' the allowable solutions; the continuous wavenumber is now replaced by an integer-valued mode number and the solution depends upon the geometry of the container. In our case, this is the aspect ratio of the cylinder.

3. Solution method

We construct a solution to the governing equation (5) by introducing the scalar potentials (ϕ, ψ, ζ) and expanding the displacement using the toroidal–poloidal decomposition,

$$\mathbf{u} = \nabla\phi + \nabla \times (\psi \hat{\boldsymbol{e}}_z) + \nabla \times \nabla \times (\zeta \hat{\boldsymbol{e}}_z). \tag{9}$$

This particular decomposition was chosen such that the shape modes ϕ, ζ and torsional modes ψ decouple [37]. Substituting (9) into (5) yields set of uncoupled Helmholtz equations,

$$\nabla^2\phi - k_1^2\phi = 0,\ \nabla^2\psi - k_2^2\psi = 0,\ \nabla^2\zeta - k_2^2\zeta = 0, \tag{10}$$

where $k_1 = s\sqrt{\frac{\rho}{\lambda+2\tilde{\mu}}}$, and $k_2 = s\sqrt{\frac{\rho}{\tilde{\mu}}}$. The general solution of (10) is given by

$$\phi = \left(A\cosh\left(\sqrt{k_1^2+k^2}\right)z + B\sinh\left(\sqrt{k_1^2+k^2}\right)z\right)J_n(kr)e^{in\theta}, \tag{11a}$$

$$\psi = \left(C\cosh\left(\sqrt{k_2^2+k^2}\right)z + D\sinh\left(\sqrt{k_2^2+k^2}\right)z\right)J_n(kr)e^{in\theta}, \tag{11b}$$

$$\zeta = \left(E\cosh\left(\sqrt{k_2^2+k^2}\right)z + F\sinh\left(\sqrt{k_2^2+k^2}\right)z\right)J_n(kr)e^{in\theta}, \tag{11c}$$

where n is the polar mode number, k the radial wavenumber, and J_n the Bessel function of order n.

3.1. Non-dimensionalization

Lengths are scaled by the thickness h and time by elastic wave time scale $\sqrt{\rho h^2/\mu}$. Applying these scalings to the governing equations give rise to the following dimensionless quantities,

$$\begin{aligned}
&\eta = sh\sqrt{\frac{\rho}{\mu}},\ \kappa = kh,\ \Gamma_1 = \sqrt{\frac{\tilde{\nu}^2\eta^2}{1+(\tau\eta)^n} + \kappa^2},\\
&\Gamma_2 = \sqrt{\frac{\eta^2}{1+(\tau\eta)^n} + \kappa^2},\\
&\tilde{\nu} = \sqrt{\frac{1-2\nu}{2(1-\nu)}},\ \alpha = \frac{\rho g h}{\mu},\ \Sigma = \frac{\sigma}{\mu h},\ \tau = t_v\sqrt{\frac{\mu}{\rho h^2}},\\
&\tilde{\mu} = \mu(1+(\tau\eta)^n).
\end{aligned} \tag{12}$$

Here η is the non-dimensional growth rate, κ the scaled wavenumber, and $\tilde{\nu}$ a compressibility factor that ranges between $\tilde{\nu} = 0$ for an incompressible $\nu = 1/2$ material and $\tilde{\nu} = 1/\sqrt{2}$ for a fully compressible $\nu = 0$ material. Three dimensionless numbers appear; α the elastogravity number and Σ the elastocapillary number, which represent the competition between gravity and capillarity with elasticity, respectively, and τ the solid Deborah number that is a measure of the relaxation time of the material with $\tau = 0$ corresponding to the purely elastic limit.

Applying the scalings to (11) and substituting these into the boundary conditions (7) & (8) delivers a set of linear equations for the unknown coefficients A, B, C, D, E, F. Solutions to these equations can be decomposed into torsional modes and shape change modes. Our interest is stability and therefore we focus on the shape change modes. For reference, we simply state the result for torsional modes and do not discuss further.

3.2. Torsional modes

The equations for the coefficients C, D associated with the potential ψ decouple,

$$C\cosh\Gamma_2 + D\sinh\Gamma_2 = 0, \qquad D\Gamma_2 = 0, \tag{13}$$

and the solvability condition gives the following dispersion relationship for the torsional modes, $\Gamma_2\cosh\Gamma_2 = 0$. These admit oscillatory solutions $\eta = \pm i\kappa$.

3.3. Shape-change modes

The equations for the remaining coefficients A, B, E, F are given by,

$$A\cosh\Gamma_1 + B\sinh\Gamma_1 + E\Gamma_2\sinh\Gamma_2 + F\Gamma_2\cosh\Gamma_2 = 0, \tag{14a}$$

$$A\Gamma_1\sinh\Gamma_1 + B\Gamma_1\cosh\Gamma_1 + E\kappa^2\cosh\Gamma_2 + F\kappa^2\sinh\Gamma_2 = 0, \tag{14b}$$

$$2B\Gamma_1 + E(\Gamma_2^2+\kappa^2) = 0, \tag{14c}$$

$$(\Gamma_2^2+\kappa^2)A + 2F\kappa^2\Gamma_2 + B\Gamma_1\frac{(\alpha-\Sigma\kappa^2)}{1+(\tau\eta)^n} + E\kappa^2\frac{(\alpha-\Sigma\kappa^2)}{1+(\tau\eta)^n} = 0. \tag{14d}$$

The solvability condition for the linear system in (14) is

$$\begin{aligned}
&4\Gamma_1\Gamma_2\kappa^2(\Gamma_2^2+\kappa^2) - \kappa^2\left(4\Gamma_1^2\Gamma_2^2 + (\Gamma_2^2+\kappa^2)^2\right)\sinh\Gamma_1\sinh\Gamma_2\\
&- \Gamma_1\Gamma_2\cosh\Gamma_1\cosh\Gamma_2(\Gamma_2^4 + 2\Gamma_2^2\kappa^2 + 5\kappa^4)\\
&\Gamma_1(\Gamma_2^2-\kappa^2)\frac{\alpha-\Sigma k^2}{1+(\tau\eta)^n}(\Gamma_1\Gamma_2\sinh\Gamma_1\cosh\Gamma_2\\
&- \kappa^2\cosh\Gamma_1\sinh\Gamma_2) = 0.
\end{aligned} \tag{15}$$

Note that the polar mode number n does not appear for the semi-infinite layer case and the wavenumber κ is continuous. This is sometimes referred to as the high wavenumber limit $\kappa \gg 1$ that corresponds to the case of an infinitely wide two-dimensional Cartesian geometry. For reference, the solution for the Cartesian system is given in Appendix B.

4. Results

Eq. (15) is a nonlinear equation that can be solved numerically to yield the dispersion relationship $\eta = \eta(\kappa)$, as it depends upon the dimensionless numbers $\alpha, \Sigma, \tilde{\nu}, \tau, n$. We report our results in terms of the square of the growth rate η^2 with the understanding that $\eta^2 > 0$ corresponds to instability and $\eta^2 < 0$ corresponds to stability (i.e. oscillations). Our focus is on instability. We focus our presentation on the results for a purely elastic material $\tau = 0$ and later show the effect of viscoelasticity on the instability.

4.1. Dispersion relation

Fig. 2 plots dispersion curves, growth rate squared η^2 against wavenumber κ, as they depend upon the dimensionless numbers $\alpha, \Sigma, \tilde{\nu}$. Each curve displays a range of unstable wavenumbers $\kappa \in [\kappa_{min}, \kappa_s]$ that can destabilize the base-state with κ_s the static limit. Each curve also exhibits a fastest growing mode distinguished by a wavenumber κ_m and growth rate η_m^2. The quantities $\kappa_s, \kappa_m, \eta_m^2$ define the dispersion relationship.

An incompressible solid $\tilde{\nu} = 0$ without surface tension $\Sigma = 0$ is unstable, as shown in Fig. 2(a). This limiting case has been previously reported by Mora et al. [28] using an energy analysis showing that the system becomes unstable at $\alpha = 6.22$ with associated wavenumber $\kappa = 2.12$. This illustrates the competition

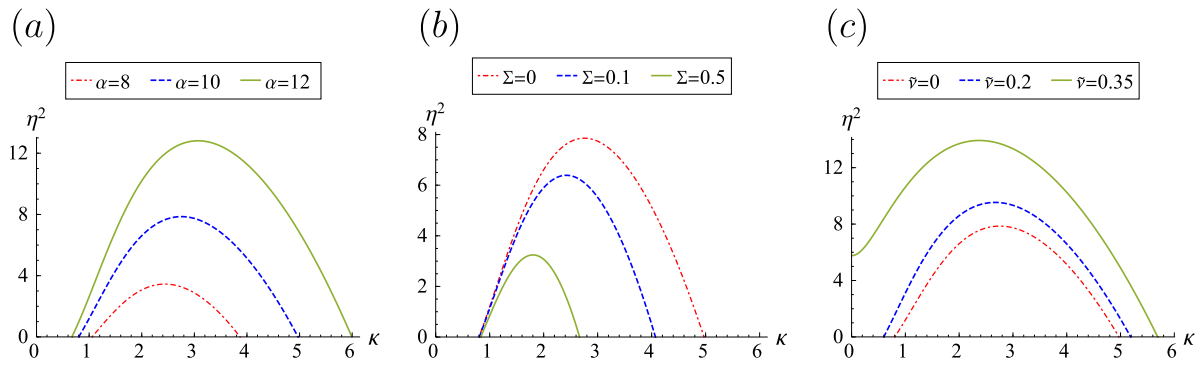

Fig. 2. Dispersion relation for a purely elastic material $\tau = 0$ plotting the squared growth rate η^2 against scaled wavenumber κ, as it depends upon (a) the elastogravity number α (fixed $\tilde{\nu} = \Sigma = 0$), (b) the elastocapillary number Σ (fixed $\alpha = 10$, $\tilde{\nu} = 0$), and (c) compressibility number $\tilde{\nu}$ (fixed $\alpha = 10$, $\Sigma = 0$).

between elastic energy and surface energy. We recover this static stability limit, as could be expected. Increasing the elastogravity number α further destabilizes, increasing both the range of unstable wavenumbers and the growth rate, and shifting κ_m to higher wavenumbers (cf. Fig. 2(a)). Surface tension tends to stabilize the system, as shown in Fig. 2(b), and is most pronounced for high wavenumbers. This is best illustrated by the large decrease in κ_s with increased Σ. In contrast, the onset wavenumber κ_{min} is relatively unaffected by Σ. Increasing the compressibility $\tilde{\nu}$ similarly tends to destabilize as shown in Fig. 2(c). In contrast to destabilization due to increased α, increasing $\tilde{\nu}$ shifts κ_m to lower wavenumbers and can also destabilize the long wavelength $\kappa = 0$ disturbances.

Most soft gels of practical interest are considered incompressible [38]. Hence, we focus the remaining presentation on this limit $\tilde{\nu} = 0$. Wavenumber selection is determined by the fastest growing mode and Fig. 3(a, b) plots η_m^2 and κ_m, as they depend upon the elastogravity α and elastocapillary Σ numbers, respectively. These plots provide a means to identify the dominant mode in experiment and the time scale on which to observe the instability. As discussed earlier, increases in Σ tend stabilize by shifting κ_m to lower wavenumbers and decreasing the growth rate η_m^2. The opposite is true for increasing α which is destabilizing. Similarly, increasing the compressibility $\tilde{\nu}$ is also destabilizing and reduces the threshold α for fixed Σ, as shown in Fig. 3(c).

4.2. Finite-size effects and mode selection

In the previous Section 4.1 we focused on the high wavenumber limit $\kappa \gg 1$ where κ was continuous and the dispersion relationship was independent of container geometry. This geometry becomes important when the disturbance wavelength $\lambda = 1/\kappa$ is the same order as the container size, in which case κ can no longer be considered continuous and takes on discrete values determined by the lateral boundary conditions at the container edge. Accordingly, we introduce the no-penetration condition at the side wall $u_r = 0$. This gives the following relationship for κ,

$$\kappa\tilde{R}J_{n-1}(\kappa\tilde{R}) - nJ_n(\kappa\tilde{R}) = 0, \tag{16}$$

where $\tilde{R} = R/h$ is the container aspect ratio. The complementary boundary condition is one with free-slip in the vertical direction $\partial u_z/\partial r = 0$ which generates the same condition as in (16). These are the natural boundary conditions. For reference, the condition for the torsional mode is $J_n(\kappa\tilde{R}) = 0$.

Note the presence of the polar mode number n in Eq. (16), which admits a discrete set of solutions κ that can be numerically ordered such that a radial mode number m can be defined. Each mode can then be defined by the mode number pair (m, n) with growth rate that depends upon the aspect ratio $\tilde{R}$. Note the polar mode number $n = 0, 1, \ldots, \infty$ and the radial mode number $m = 1, 2, \ldots, \infty$. Fig. 4(a) plots η^2 against the aspect ratio $\tilde{R}$ for the dominant modes with $\alpha = 10$, $\Sigma = 0$, $\tilde{\nu} = 0$ in that range of $\tilde{R}$. For a given aspect ratio $\tilde{R}$, there is always a single dominant mode with fastest growth rate except when two curves intersect at which point there are two modes both of which have the fastest growth rate. In this region, hysteresis and nonlinear effects can be expected to be important in mode number selection. For increasing $\tilde{R}$, modes tend to become bunched together and the range of $\tilde{R}$ for which a particular mode is dominant becomes smaller. Eventually, for large $\tilde{R} \gg 1$ the effect of container geometry is lost and κ can be assumed to be continuous. Mode selection is dictated by the fastest growing mode and Fig. 4(b) shows a mode selection diagram as it depends upon $\tilde{R}$. For each $\tilde{R}$, the dominant mode can be easily read off of Fig. 4(b). For small $\tilde{R} < 2$, the $m = 1$ modes are selected and the range of $\tilde{R}$ for a given mode is relatively large, particularly for the (1,1) mode. For large aspect ratios $\tilde{R} > 3$, modes tend to switch order quite frequently indicating possible clustering of many modes close to the maximum growth rate. In these regions, mode selection could be influenced by small imperfections in experimental conditions, i.e. small variations in height or gel shear modulus, and may even become statistical. The mode selections diagrams in Fig. 4(c, d) shows that changing Σ and α does not change the ordering of modes, but rather the range of $\tilde{R}$ over which they appear. For example, increasing Σ tends to expand the range of $\tilde{R}$ for a given mode (cf. Fig. 4(c)), whereas increasing α shrinks the range $\tilde{R}$ (cf. Fig. 4(d)) and leads to clustering of modes within small ranges of $\tilde{R}$.

A given mode (m, n) will achieve its maximum growth rate and become the dominant mode at a critical aspect ratio R^*, as shown in Fig. 4(a). Naturally, R^* can be expected to depend upon the dimensionless numbers α, Σ, $\tilde{\nu}$. Fig. 5(a, b) shows how R^* changes with α and Σ, respectively. Near the stability threshold $\alpha = 6.22$, R^* achieves its maximum value and decreases monotonically with increasing α for a given mode. For a given α, any mode can be accessed by changing the aspect ratio $\tilde{R}$. This is seen by traversing the graph in Fig. 5(a) vertically. However, for a fixed $\tilde{R}$ it is not possible to access any mode by changing the elastogravity number α, e.g. for $\tilde{R} = 3$, the (1,1), (1,0) modes are not accessible for any α, as seen by traversing Fig. 5(a) horizontally. For large α, the modes tend to cluster in a small range of $\tilde{R}$ and here small changes in $\tilde{R}$ can lead to significant changes in mode selection. Fig. 5(b) shows the elastocapillary number Σ has the opposite effect on R^*, i.e. R^* increases with increasing Σ. Similarly, for fixed aspect ratio $\tilde{R}$ it may not be possible to access any mode, e.g. for $\tilde{R} = 2$, the (3,1) mode cannot be observed for any Σ and some modes might be stable. This is a signature of pattern formation with finite-size effects.

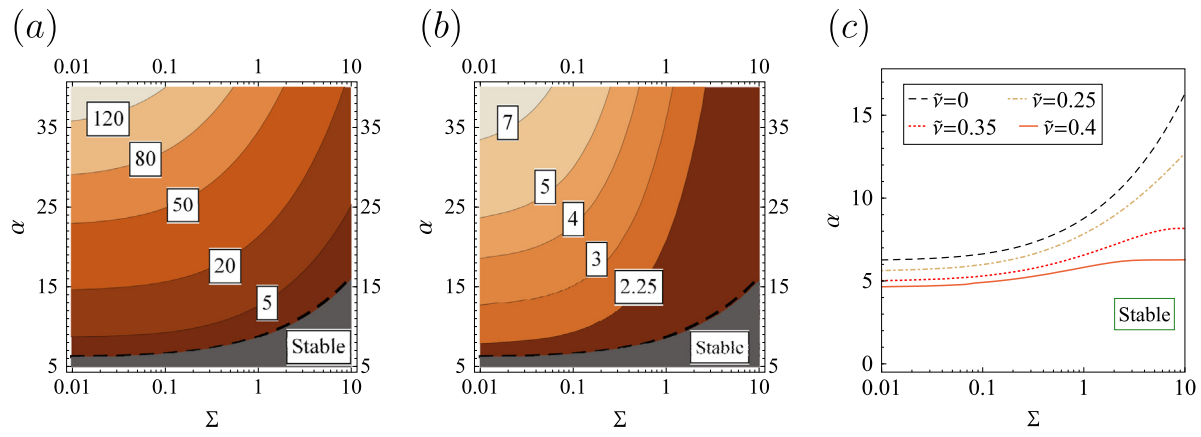

Fig. 3. (*a*) Maximum growth rate squared η_m^2, (*b*) wavenumber at maximum growth κ_m, and (*c*) static stability limit κ_s, as they depend upon elastogravity α and elastocapillary Σ numbers for an incompressible purely elastic material ($\tilde{\nu} = 0, \tau = 0$). Dashed line in sub-figures (a, b) denotes the stability boundary. (*c*) Stability diagram for a given compressibility $\tilde{\nu}$ separates stable and unstable regions in the $\alpha - \Sigma$ parameter space.

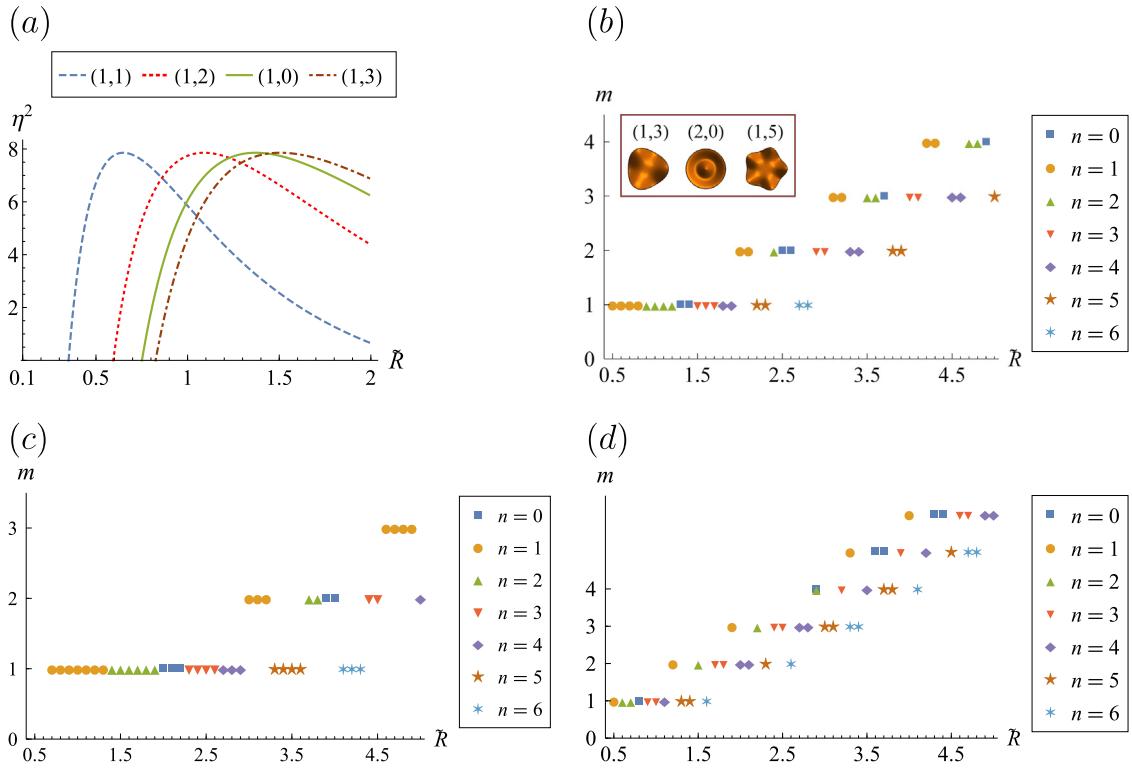

Fig. 4. Mode selection for incompressible purely elastic material ($\tilde{\nu} = 0, \tau = 0$). (*a*) Growth rate squared η^2 against aspect ratio $\tilde{R}$ for modes (m, n) with $\alpha = 10$, $\Sigma = 0$ shows a dominant mode for each $\tilde{R}$. (b, c, d) Dominant modes are mapped against aspect ratio $\tilde{R}$ for (*b*) $\alpha = 10$, $\Sigma = 0$, (*c*) $\alpha = 10$, $\Sigma = 0.5$, and (*d*) $\alpha = 20$, $\Sigma = 0$.

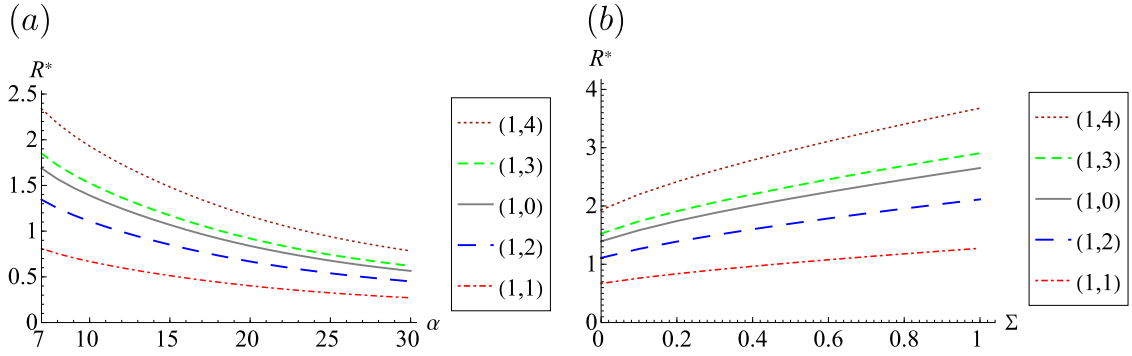

Fig. 5. Critical aspect ratio R^* against (*a*) elastogravity number α ($\Sigma = 0$) and (*b*) elastocapillary number Σ ($\alpha = 10$) for an incompressible purely elastic material ($\tilde{\nu} = 0, \tau = 0$).

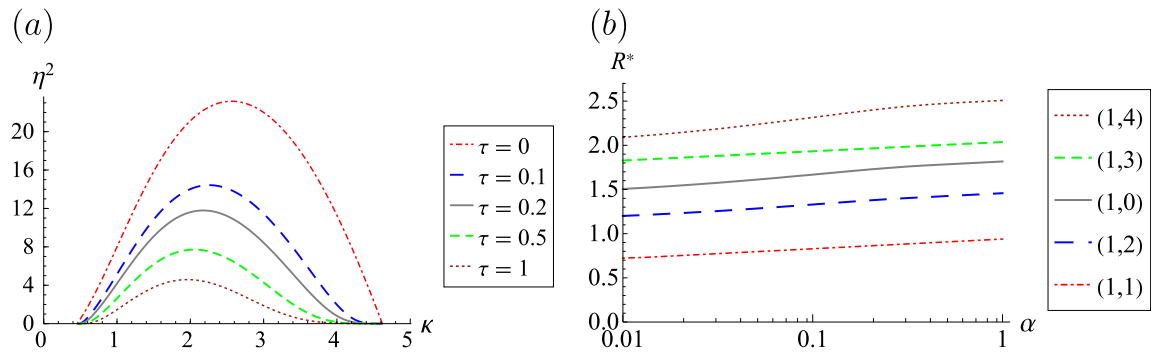

Fig. 6. Viscoelastic effects illustrated in the (a) dispersion relationship plotting η^2 against κ, as it depends upon the solid Deborah number τ for $\alpha = 20, \sigma = 0.5, \tilde{\nu} = 0, n = 0.5$ and (b) critical aspect ratio R^* again τ for $\alpha = 10, \Sigma = 0, \tilde{\nu} = 0, n = 0.5$.

4.3. Comparison with experiment

Our analysis presented in the previous section can be compared with recent experimental observations of gravity-driven instabilities of soft elastic layers in cylindrical containers [28,32]. Zheng et al. [32] have observed the (1,1) and (1,0) modes on soft hydrogels with $\mu = 32$ Pa in containers which correspond to $\alpha = 10.26$ and $\tilde{R} = 0.7$. For $\tilde{\nu} = 0$ and $\Sigma = 0$, the model predictions shown in Fig. 4(b) for $\alpha = 10$ are close to those experimental conditions and it is clearly seen that the (1,1) is the dominant mode for this set of parameters. In addition, they also observed the (1,0) mode for the same set of parameters indicating a coexistence of dominant modes. Our predictions in Fig. 4(b) show the (1,0) mode is the dominant mode for larger $\tilde{R}$. This discrepancy between experiment and our model could be caused by a number of factors including (i) nonlinear effects due to large deformations [27,29], (ii) nonlinear saturation of a given mode, or (iii) surface tension effects. Mora et al. [28] observed similar coexistence phenomena including three different mode patterns for fixed experimental conditions and attributed this observation to uncontrollable inhomogeneities in both space and time. Their experimental conditions were performed for higher aspect ratio containers $\tilde{R} = 3.23$ and we find agreement between the experiment with $\alpha = 6.3$ and our model predictions for the (2,0) mode [28, Fig. 2d]. Other experiments with $\alpha = 6.74$ [28, Figs. 2e,2f,2g] produce modes with higher polar mode numbers $n = 3, 4, 6$, respectively, for the same experimental conditions and we note our model predicts the dominant modes, (2,3), (2,4), and (1,6), for slightly larger aspect ratio $\tilde{R} > 3.23$. In any case, it is clear that mode number selection is sensitive in this system and more comprehensive modeling and experiments could be done to further investigate modal coexistence and possible hysteresis.

4.4. Viscoelastic effects

Fig. 6(a) shows how viscoelasticity affects the dispersion relationship through the solid Deborah number τ. Here increasing τ has a damping effect as κ_m is shifted to smaller wavenumber and the growth rate η decreases. Note that the range of unstable wavenumbers κ_s is not affected by viscoelasticity. This is similar to viscous damping in fluids [39]. The effect of τ on the critical aspect ratio R^* for the dominant modes is shown in Fig. 6(b). Here R^* increases with τ for a fixed mode number and the ordering of the modes remain unchanged.

5. Concluding remarks

We have derived a dispersion relationship for the gravity-driven instability of a soft viscoelastic layer in a cylindrical container, which depends upon gravity, surface tension, compressibility, viscoelasticity, and geometry through the following non-dimensional numbers: elastogravity number α, elastocapillary number Σ, compressibility $\tilde{\nu}$, solid Deborah number τ, and aspect ratio $\tilde{R}$. Solutions to the governing elastodynamic equations are defined by the mode number pair (m, n) with associated growth rate η. For large aspect ratio $\tilde{R} \gg 1$, the modes are no longer discrete but defined by a continuous wavenumber κ. Gravity destabilizes the system to a range of unstable wavenumbers that define static stability, whereas surface tension is a stabilizing force that shrinks this range. Our dynamic analysis is distinguished from static analysis in that we predict the most unstable wavenumber κ_m with maximum growth rate η_m. This distinction is important as this mode is the one to be observed in experiment. For finite-sized containers, we give model predictions for mode selection (cf. Figs. 4, 5) and these predictions show good agreement with prior experimental results [28,32].

Again, gravity and surface tension plays a role in this mechanism where a particular mode is selected at increasingly lower aspect ratio with increasing gravitational acceleration, higher aspect ratios with increasing surface tension effects. We find that our model only predicts one of the observed modes as the dominant one. This points to possible nonlinear effects playing a role in determining the dominant modes. Viscoelasticity also plays a role in defining the critical aspect ratio for that particular mode.

Our model gives a simple, yet elegant, mode selection mechanism for Rayleigh–Taylor instability in soft viscoelastic solids with finite surface tension and compressibility. Future model extensions could include nonlinear effects and detailed analysis of mode selection in regions which exhibit modal coexistence and perhaps hysteresis. It is also possible to consider other configurations for the Rayleigh–Taylor instability in solids, such as multiple layers of varying density (heavy over light). For the case of two materials, previous studies have noted that this introduces the Atwood number $\mathrm{At} \equiv \frac{\rho_1 - \rho_2}{\rho_1 + \rho_2}$ [24], which is a non-dimensional density difference that varies between 0 to 1. Our model corresponds to the limiting case $\mathrm{At} = 1$. Smaller values of At tend to damp the instability growth rate. The number of non-dimensional parameters will increase significantly when considering multiple layers with unique material properties.

Lastly, we note that it may be possible to develop a quick and inexpensive method to estimate the surface tension of soft gels by simply correlating experimental observations to our model treating surface tension σ as a fit parameter. This is something that is critically needed for the field of elastocapillarity and is important because the typical surface tension measurement methods for liquids, e.g. Wilhelmy plate, du Nuoy ring, pendant drop, do not work for gels. Other researchers have recently applied this approach to mechanically-excited Faraday waves [40], oscillating gel drops [41,42], and the characterization of the wetting ridge geometry at the contact-line (i.e. Neumann's triangle) [43–45], to name a few. The advantage of the gravity-driven instability approach over the previously mentioned techniques is that no

sophisticated or expensive lab equipment is required, thus making this a true table-top technique. Nonlinearity in soft gels can undergo strain stiffening [46] which could affect the instability shape and therefore this proposed technique. However, our analysis for small strains agrees reasonably well with experiment and therefore the current model could be a useful predictor of the surface tension of soft gels. Future experiments could be designed to further explore this area.

Declaration of competing interest

The authors declare that they have no known competing financial interests or personal relationships that could have appeared to influence the work reported in this paper.

Acknowledgments

We would like to thank an anonymous referee for suggesting we extend our model to include viscoelastic effects. JBB acknowledges support from National Science Foundation, United States of America Grant CBET-1750208.

Appendix A. Cylindrical field components

The general solution for the potential functions (ϕ, ψ, ζ) is given by Eq. (11). The corresponding components of displacement are given by

$$u_r = [A\cosh az + B\sinh az + b\,(E\sinh bz + F\cosh bz)]\left(kJ_{n-1}(kr) - \frac{n}{r}J_n(kr)\right)e^{in\theta} + \frac{in}{r}[C\cosh bz + D\sinh bz]J_n(kr)e^{in\theta} \tag{A.1a}$$

$$u_\theta = \frac{in}{r}[A\cosh az + B\sinh az + b(E\cosh bz + F\sinh bz)]J_n(kr)e^{in\theta} \tag{A.1b}$$

$$- [C\cosh bz + D\sinh bz]\left(kJ_{n-1}(kr) - \frac{n}{r}J_n(kr)\right)e^{in\theta} \tag{A.1c}$$

$$u_z = [b\,(A\cosh az + B\sinh az) + k^2\,(E\cosh bz + F\sinh bz)] \times J_n(kr)e^{in\theta}, \tag{A.1d}$$

where $a = \sqrt{k_1^2 + k^2}$, $b = \sqrt{k_2^2 + k^2}$. Similarly, the components of stress are given by

$$\tau_{zz} = 2\tilde{\mu}\left[\frac{b^2 + k^2}{2}(A\cosh az + B\sinh az) + bk^2(E\cosh bz + F\cosh bz)\right]J_n(kr)e^{in\theta} \tag{A.2a}$$

$$\tau_{rz} = \tilde{\mu}\left[\left(2b(A\sinh az + B\cosh az) + (b^2 + k^2)\right) \times (E\cosh bz + F\cosh bz)\right)\left(kJ_{n-1}(kr) - \frac{n}{r}J_n(kr)\right) + \frac{inb}{r}(C\sinh bz + D\cosh bz)\Bigg]e^{in\theta} \tag{A.2b}$$

$$\tau_{\theta z} = \tilde{\mu}\left[\frac{in}{r}\{2a(A\sinh az + B\cosh az) + (b^2 + k^2) \times (E\cosh bz + F\sinh bz)\}\right.$$

$$\left. J_n(kr) - b(C\sinh bz + D\cosh bz)\left(kJ_{n-1}(kr) - \frac{n}{r}J_n(kr)\right)\right]e^{in\theta}. \tag{A.2c}$$

Appendix B. Dispersion relation for the Cartesian system

The analysis presented here for the purely elastic $\tau = 0$ case can be readily adapted to a 2D Cartesian system with corresponding displacement field $\mathbf{u}(x, y) = u_x(x, y)\hat{e}_x + u_y(x, y)\hat{e}_y$ which obeys the governing equation (5). Here we take following decomposition

$$\mathbf{u}(x, y) = \nabla\Phi + \nabla \times \Psi, \tag{B.1}$$

which admits general solutions for the potential Φ, Ψ,

$$\Phi = (A_1\cosh ay + A_2\sinh ay)e^{ikx}, \tag{B.2a}$$

$$\Psi = (B_1\sinh by + B_2\cosh by)e^{ikx}, \tag{B.2b}$$

where k is the wavenumber with the symbols having been defined previously. Applying (B.2) to the equivalent displacement (7) and stress (8) boundary conditions at $y = 0$ and $y = h$, respectively, we get the following linear systems of equations for the unknowns A_1, A_2, B_1, B_2,

$$ik(A_1\cosh\Gamma_1 + A_2\sinh\Gamma_1) + \Gamma_2(B_1\cosh\Gamma_2 + B_2\sinh\Gamma_2) = 0, \tag{B.3a}$$

$$\Gamma_1(A_1\sinh\Gamma_1 + A_2\cosh\Gamma_1) - ik(B_1\sinh\Gamma_2 + B_2\cosh\Gamma_2) = 0, \tag{B.3b}$$

$$2ik A_2 + (\Gamma_2^2 + \kappa^2)B_2 = 0. \tag{B.3c}$$

$$(\Gamma_2^2 + \kappa^2)A_1 - 2ik\Gamma_2 B_1 + \frac{(\alpha - \Sigma\kappa^2)}{1 + (\tau\eta)^n}(\Gamma_1 A_2 - ikB_2) = 0. \tag{B.3d}$$

The solvability condition for this system of equations gives,

$$4\Gamma_1\Gamma_2\kappa^2(\Gamma_2^2 + \kappa^2) + \frac{(\alpha - \Sigma\kappa^2)}{1 + (\tau\eta)^n}\Gamma_1^2\Gamma_2(\Gamma_2^2 - \kappa^2)\sinh\Gamma_1\cosh\Gamma_2 - \Gamma_1\Gamma_2(\Gamma_2^4 + 2\Gamma_2^2\kappa^2 + 5\kappa^2)\cosh\Gamma_1\cosh\Gamma_1 - \frac{(\alpha - \Sigma\kappa^2)}{1 + (\tau\eta)^n}\Gamma_1\kappa^2(\Gamma_2^2 - \kappa^2)\cosh\Gamma_1\sinh\Gamma_2 + \kappa^2(4\Gamma_1^2\Gamma_2^2 + (\Gamma_2^2 + \kappa^2)^2\sinh\Gamma_1\sinh\Gamma_2) = 0 \tag{B.4}$$

from which the dispersion relationship can be computed.

References

[1] G. Foyart, L. Ramos, S. Mora, C. Ligoure, The fingering to fracturing transition in a transient gel, Soft Matter 9 (32) (2013) 7775–7779.
[2] M. Grzelka, J.B. Bostwick, K.E. Daniels, Capillary fracture of ultrasoft gels: variability and delayed nucleation, Soft Matter 13 (16) (2017) 2962–2966.
[3] R.W. Style, R. Boltyanskiy, Y. Che, J. Wettlaufer, L.A. Wilen, E.R. Dufresne, Universal deformation of soft substrates near a contact line and the direct measurement of solid surface stresses, Phys. Rev. Lett. 110 (6) (2013) 066103.
[4] J.B. Bostwick, M. Shearer, K.E. Daniels, Elastocapillary deformations on partially-wetting substrates: rival contact-line models, Soft Matter 10 (37) (2014) 7361–7369.
[5] S. Park, J. Bostwick, V. De Andrade, J. Je, Self-spreading of the wetting ridge during stick–slip on a viscoelastic surface, Soft Matter 13 (44) (2017) 8331–8336.
[6] J. Dervaux, M.B. Amar, Mechanical instabilities of gels, Annu. Rev. Condens. Matter Phys. 3 (1) (2012) 311–332.
[7] B. Li, Y.-P. Cao, X.-Q. Feng, H. Gao, Mechanics of morphological instabilities and surface wrinkling in soft materials: a review, Soft Matter 8 (21) (2012) 5728–5745.
[8] B. Andreotti, J.H. Snoeijer, Statics and dynamics of soft wetting, Annu. Rev. Fluid Mech. 52 (2020).

[9] R.W. Style, A. Jagota, C.-Y. Hui, E.R. Dufresne, Elastocapillarity: Surface tension and the mechanics of soft solids, Annu. Rev. Condens. Matter Phys. 8 (2017) 99–118.
[10] J. Bico, É. Reyssat, B. Roman, Elastocapillarity: When surface tension deforms elastic solids, Annu. Rev. Fluid Mech. 50 (2018) 629–659.
[11] S. Mora, T. Phou, J.-M. Fromental, L.M. Pismen, Y. Pomeau, Capillarity driven instability of a soft solid, Phys. Rev. Lett. 105 (21) (2010) 214301.
[12] M. Taffetani, P. Ciarletta, Beading instability in soft cylindrical gels with capillary energy: weakly non-linear analysis and numerical simulations, J. Mech. Phys. Solids 81 (2015) 91–120.
[13] R. Alert, C. Blanch-Mercader, J. Casademunt, Active fingering instability in tissue spreading, Phys. Rev. Lett. 122 (8) (2019) 088104.
[14] S. Tamim, J. Bostwick, The elastic rayleigh drop, Soft Matter 15 (45) (2019) 9244–9252.
[15] X. Shao, S. Fredericks, J. Saylor, J. Bostwick, Elastocapillary transition in gel drop oscillations, Phys. Rev. Lett. 123 (18) (2019) 188002.
[16] Rayleigh, Investigation of the character of the equilibrium of an incompressible heavy fluid of variable density, Proc. Lond. Math. Soc. s1-14 (1) 170–177, http://dx.doi.org/10.1112/plms/s1-14.1.170.
[17] G.I. Taylor, The instability of liquid surfaces when accelerated in a direction perpendicular to their planes. i, Proc. R. Soc. Lond. Ser. A Math. Phys. Sci. 201 (1065) (1950) 192–196.
[18] G.A. Houseman, P. Molnar, Gravitational (rayleigh–taylor) instability of a layer with non-linear viscosity and convective thinning of continental lithosphere, Geophys. J. Int. 128 (1) (1997) 125–150.
[19] P. Mondal, J. Korenaga, A propagator matrix method for the rayleigh–taylor instability of multiple layers: a case study on crustal delamination in the early earth, Geophys. J. Int. 212 (3) (2018) 1890–1901.
[20] S.A. Colgate, R.H. White, The hydrodynamic behavior of supernovae explosions, Astrophys. J. 143 (1966) 626.
[21] Y. Sun, A. Piriz, Magneto-rayleigh-taylor instability in solid media, Phys. Plasmas 21 (7) (2014) 072708.
[22] J. Miles, General dynamics report no, GAMD-7335, AD 643161, 1966.
[23] J.L. Cela, A. Piriz, M.S. Moreno, N. Tahir, Numerical simulations of rayleigh-taylor instability in elastic solids, Laser Part. Beams 24 (3) (2006) 427–435.
[24] A. Piriz, J.L. Cela, O. Cortazar, N. Tahir, D. Hoffmann, Rayleigh-taylor instability in elastic solids, Phys. Rev. E 72 (5) (2005) 056313.
[25] A. Piriz, J.L. Cela, N. Tahir, Linear analysis of incompressible rayleigh-taylor instability in solids, Phys. Rev. E 80 (4) (2009) 046305.
[26] A. Piriz, J.L. Cela, N. Tahir, Rayleigh–taylor instability in elastic–plastic solids, 2009.
[27] D. Riccobelli, P. Ciarletta, Rayleigh–taylor instability in soft elastic layers, Phil. Trans. R. Soc. A 375 (2093) (2017) 20160421.
[28] S. Mora, T. Phou, J.-M. Fromental, Y. Pomeau, Gravity driven instability in elastic solid layers, Phys. Rev. Lett. 113 (17) (2014) 178301.
[29] A. Chakrabarti, S. Mora, F. Richard, T. Phou, J.-M. Fromental, Y. Pomeau, B. Audoly, Selection of hexagonal buckling patterns by the elastic rayleigh-taylor instability, J. Mech. Phys. Solids 121 (2018) 234–257.
[30] H. Yu, D. Livescu, Rayleigh–taylor instability in cylindrical geometry with compressible fluids, Phys. Fluids 20 (10) (2008) 104103.
[31] H. Sweeney, R. Kerswell, T. Mullin, Rayleigh–taylor instability in a finite cylinder: linear stability analysis and long-time fingering solutions, J. Fluid Mech. 734 (2013) 338–362.
[32] Y. Zheng, Y. Lai, Y. Hu, S. Cai, Rayleigh–taylor instability in a confined elastic soft cylinder, J. Mech. Phys. Solids 131 (2019) 221–229.
[33] R. Christensen, Theory of Viscoelasticity: An Introduction, Elsevier, 2012.
[34] H.H. Winter, F. Chambon, Analysis of linear viscoelasticity of a crosslinking polymer at the gel point, J. Rheol. 30 (2) (1986) 367–382.
[35] F. Chambon, H.H. Winter, Linear viscoelasticity at the gel point of a crosslinking pdms with imbalanced stoichiometry, J. Rheol. 31 (8) (1987) 683–697.
[36] S. Karpitschka, S. Das, M. van Gorcum, H. Perrin, B. Andreotti, J.H. Snoeijer, Droplets move over viscoelastic substrates by surfing a ridge, Nature Commun. 6 (1) (2015) 1–7.
[37] A. Eringer, E. Suhubi, Elastodynamics, Vol. 2, Academic Press, New York, 1975.
[38] J.B. Bostwick, K.E. Daniels, Capillary fracture of soft gels, Phys. Rev. E 88 (4) (2013) 042410.
[39] M.S. Plesset, C.G. Whipple, Viscous effects in rayleigh-taylor instability, Phys. Fluids 17 (1) (1974) 1–7.
[40] X. Shao, J. Saylor, J. Bostwick, Extracting the surface tension of soft gels from elastocapillary wave behavior, Soft Matter 14 (36) (2018) 7347–7353.
[41] A. Chakrabarti, M.K. Chaudhury, Direct measurement of the surface tension of a soft elastic hydrogel: exploration of elastocapillary instability in adhesion, Langmuir 29 (23) (2013) 6926–6935.
[42] X. Shao, S. Fredericks, J. Saylor, J. Bostwick, A method for determining surface tension, viscosity, and elasticity of gels via ultrasonic levitation of gel drops, J. Acoust. Soc. Am. 147 (4) (2020) 2488–2498.
[43] N. Nadermann, C.-Y. Hui, A. Jagota, Solid surface tension measured by a liquid drop under a solid film, Proc. Natl. Acad. Sci. 110 (26) (2013) 10541–10545.
[44] Q. Xu, R.W. Style, E.R. Dufresne, Surface elastic constants of a soft solid, Soft Matter 14 (6) (2018) 916–920.
[45] R.D. Schulman, M. Trejo, T. Salez, E. Raphaël, K. Dalnoki-Veress, Surface energy of strained amorphous solids, Nature Commun. 9 (1) (2018) 1–6.
[46] M. Jaspers, M. Dennison, M.F. Mabesoone, F.C. MacKintosh, A.E. Rowan, P.H. Kouwer, Ultra-responsive soft matter from strain-stiffening hydrogels, Nature Commun. 5 (1) (2014) 1–8.